nature chemistry

Article

https://doi.org/10.1038/s41557-025-02045-x

Wavelength-steered directional rotation in an autonomous light-driven molecular motor

Received: 26 July 2024

Accepted: 4 December 2025

Published online: 28 January 2026

Check for updates

Federico Nicoli[1,2,6], Chiara Taticchi[1,2,6], Emilio Lorini[1], Sara Borghi[3], Flavia Aleotti[1], Serena Silvi[2,4], Alberto Credi[1,2], Marco Garavelli[1], Luca Muccioli[1] ✉, Massimo Baroncini[2,5] ✉ & Massimiliano Curcio[1,2] ✉

Artificial molecular motors are at the forefront of research in nanotechnology due to their ability to perform tasks by harnessing directionally controlled motion at the molecular scale. The development of light-driven nanomotors is a particularly challenging task that holds great potential for the development of sunlight-powered systems and active materials. Here we describe an azoimidazolium photochemical molecular rotary motor which operates along a triangular reaction cycle exploiting the formation of diastereomeric species upon photoisomerisation. The different thermal stability and photochemical reactivity of these diastereomers permit net directional motion combining a thermal rotation about a C–N single bond and two light-induced configurational rearrangements that proceed predominantly through a rotational mechanism, as corroborated by computational studies. The composition of the dissipative state obtained upon continuous supply of light can be modified by changing the irradiation wavelength, and as a result, the preferred rotation direction of the motor is inverted.

Molecular motors are ubiquitous in living organisms, executing vital roles in processes such as energy transduction, substrate transport and mechanical actuation[1–3]. To perform such elaborate tasks, biomolecular machines continuously and autonomously dissipate energy to access and sustain states away from thermodynamic equilibrium[4,5]. Inspired by nature, the development of artificial systems able to rectify Brownian motion through external energy input is a cutting-edge challenge in modern nanoscience[6–8]. Compared with chemical and electrical stimuli[9,10], the use of light as an energy source is highly advantageous as it is widely accessible and potentially renewable, can promote clean and reversible reactions, and it is easily delivered to the substrate with excellent resolution in terms of intensity, space and duration[11,12].

Artificial light-driven molecular rotary motors involve the net directional rotation of one subunit—that is, the rotator—with respect to another—that is, the stator—achieved through the combination of photochemical and thermal reactions within a closed network[13,14]. The past two decades have seen an intense research activity centred on rotary motors based on stilbene[15–19], imine[20,21], hemithioindigo[22–25] and related[26–28] structures (Fig. 1, blue frame). The fine tuning of the parameters and efficiency of Feringa-type stilbene motors fostered their exploratory implementation in light-actuated materials[29–32] and motion-driven transport in compartmentalized systems[33–35]. Nonetheless, all the reported artificial light-driven molecular rotary motors present intrinsic limitations related to their synthetic accessibility,

[1]Dipartimento di Chimica Industriale "Toso Montanari", Alma Mater Studiorum – Università di Bologna, Bologna, Italy. [2]CLAN-Center for Light Activated Nanostructures, ISOF-CNR, Bologna, Italy. [3]Department of Chemistry, Oxford University, Oxford, UK. [4]Dipartimento di Chimica "G. Ciamician", Alma Mater Studiorum – Università di Bologna, Bologna, Italy. [5]Dipartimento di Scienze e Tecnologie Agro-Alimentari, Alma Mater Studiorum – Università di Bologna, Bologna, Italy. [6]These authors contributed equally: Federico Nicoli, Chiara Taticchi. ✉e-mail: luca.muccioli@unibo.it; massimo.baroncini@unibo.it; massimiliano.curcio@unibo.it

https://doi.org/10.1038/s41557-025-02045-x

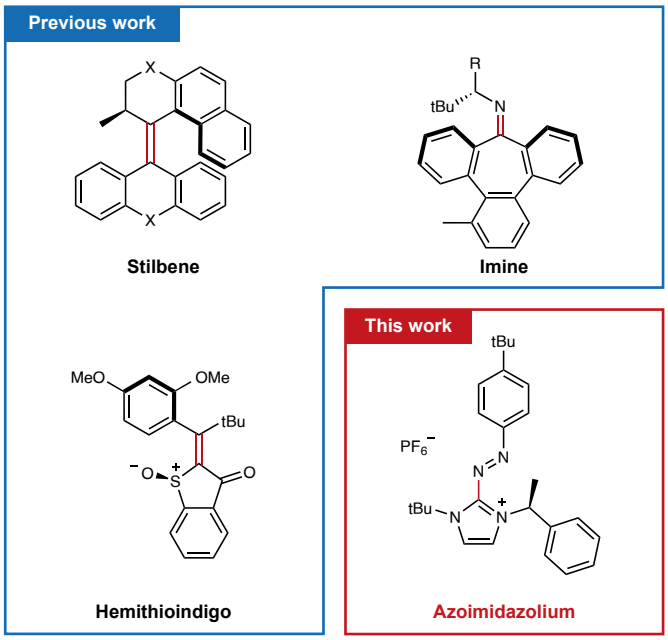

Fig. 1 | Selected artificial molecular rotary motors. The chemical structures of representative stilbene, imine and hemithioindigo rotary motors (blue frame, tBu = *tert*-butyl) and of the azoimidazolium-based molecular motor presented in this work (red frame). The bond involved in the net directional rotation is highlighted in red.

stability or efficiency of operation, which altogether hinder their broad application[36,37]. The technological innovation necessary to implement this class of molecules in advanced devices requires unexplored routes to be undertaken. Key features common to all reported light-driven rotary motors include (1) the existence of multiple accessible isomeric forms, (2) the presence of two or more combined chirality elements, (3) a closed network of photochemical and thermal reactions enabling the sequential interconversion between the isomeric forms of the motor, according to a multistep mechanism that reminds the strokes of macroscopic thermal engines.

Taking these requirements in consideration, we developed a cationic diazene photoswitch that incorporates an imidazole-based heterocyclic core (Fig. 1, red frame). Analogous to its widely studied azobenzene relative[38], such photochromic compound can efficiently interconvert between linear *E* and bent *Z* isomers upon light irradiation[39]. However, here two diastereomeric *Z* isomers are generated by the interplay between a non-symmetric substitution pattern at the endocyclic nitrogen atoms and the photogenerated axial chirality of the *Z*-diazene in combination with a fixed chiral centre.

In the following, we demonstrate that in such a system continuous illumination sustains the net directional travel along a closed reaction network through the combination of the different photoreactivity of the diastereomers and their interconversion by rotation about a single C–N bond. Autonomous directional rotation about a single bond has been reported only for a chemically fuelled rotary motor[40], whereas all the reported light-driven motors operate via rotation about double bonds. The system described here is therefore the first example of a light-driven motor that exploits the photochemical features of diazene compounds and rotation about a single bond. Importantly, the direction of the motion undertaken depends on the irradiation wavelength and inverts upon switching from ultraviolet (UV) light to visible light, a highly desirable feature unprecedented so far. The ready availability and innovative working principle of the presented motor, together with the widespread applications based on diazene derivatives[41], confer this system tremendous potential for innovation in nanotechnology.

Results and discussion

Synthetic and photophysical considerations

The adopted synthetic pathway involved the reaction of an appropriate *N*,*N*′-disubstituted imidazolium halide salt with Ag_2O to obtain the corresponding *N*-heterocyclic carbene metal complex[42], whose ligand nucleophilicity was then exploited to react with a diazonium salt to yield the desired azoimidazolium cation (Supplementary Information). Crucially, this straightforward and high-yielding synthetic strategy provides rapid access to rotary motor candidates on multigram scale.

The absorption spectra of the cationic photoswitches in chloroform show classical diazene features such as an intense π–π* absorption band at around 382 nm, which partially overlaps with a less intense band centred at around 470 nm, related to the symmetry-forbidden *n*–π* transition (Supplementary Figs. 33, 39 and 45). In all cases, irradiation at 365 nm induces *E* → *Z* isomerization, leading to a *Z*-enriched photostationary state (PSS), whereas the reverse *Z* → *E* reaction can be carried out either thermally in the dark or photochemically upon irradiation at 546 nm (Supplementary Table 1 and Supplementary Figs. 33–51). In line with previously reported *N*,*N*′-dialkylazoimidazolium compounds[43], the *Z* isomers show rapid room temperature back-isomerization reactions in the dark with $t_{½} < 10$ min (Supplementary Figs. 37, 43 and 49), which slows down to 59 h at 218 K (Supplementary Fig. 31).

Slow conformational dynamics, R1

The first condition necessary to achieve rotary motion in the presented system involves the localization of the *Z*-arylazo unit on one face of the plane identified by the imidazolium ring; in addition, such unit must be able to reach the opposite face upon rotation about the C–N single bond. To study this process, the symmetric model compound [**R1**][PF_6], bearing two identical benzylic substituents, was synthesized and investigated (Fig. 2a). In situ irradiation at 365 nm of a deuterated chloroform solution of the planar [*E*-**R1**]$^+$ provides the corresponding bent *Z* isomer, in which the arylazo group is positioned on either face of the plane identified by the imidazolium ring, leading to the formation of two sets of inequivalent benzylic protons: H_a, H_c shielded by the phenyl ring current of the arylazo group, and H_b, H_d lying on the opposite face of the molecule (Fig. 2b). These two sets of protons dynamically interconvert upon rotation of the NCNN dihedral (*Σ*) (Fig. 2a) about the C–N single bond. The exchange process was studied by variable-temperature nuclear magnetic resonance (NMR) spectroscopy, which showed that the benzylic resonance at 4.7 ppm resolves at temperatures lower than 243 K from a singlet to a pair of doublets having features proper of geminal coupling between diastereotopic benzylic protons ($^2J = 14.3$ Hz)[44] (Fig. 2c and Supplementary Fig. 24). Hence, the light-driven isomerization of the phenylazoimidazolium unit leads to a unique example of photochemically generated atropisomerism due to the slow rotation about the *Σ* dihedral. However, the molecular structure of [*Z*-**R1**]$^+$ does not induce any discrimination between the two faces—and thus no possible directionality—since (1) the rotation of the *Σ* dihedral transforms [*Z*-**R1**]$^+$ into itself and (2) the process is independent on the path undertaken by the rotation (that is, clockwise or counter clockwise).

Photogenerated axial chirality, R2

A higher degree of stereochemical control was exerted by restricting the degrees of freedom of the system. To this aim, one of the benzylic substituents of the imidazolium unit was replaced by a sterically demanding *tert*-butyl group, leading to [**R2**][PF_6] (Fig. 3a). As for the symmetric dibenzyl relative, irradiation at 365 nm converts [*E*-**R2**]$^+$ into the corresponding *Z* isomer (Supplementary Fig. 25), which exists as a mixture of enantiomers. The arylazo unit in [*Z*-**R2**]$^+$ can now rotate about the central C–N single bond according to two pathways having different activation energy, due to the different steric hindrance between the *tert*-butyl and the benzylic substituents, which translates into a preferential dihedral rotation through the lower energy benzylic path (Fig. 3b,c). The complete reaction network describing

https://doi.org/10.1038/s41557-025-02045-x

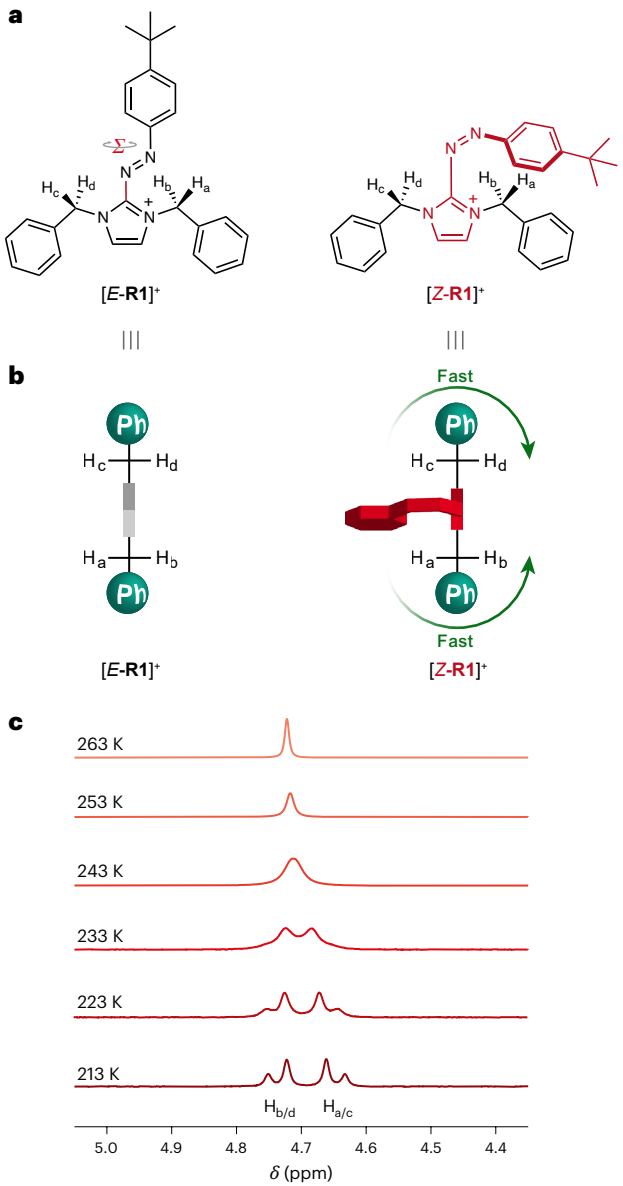

Fig. 2 | Spatial orientation and slow dihedral rotation in the symmetric compound [R1]$^+$. a, Molecular structures. **b**, Top-view cartoon projections of [*E*-**R1**]$^+$ and [*Z*-**R1**]$^+$. The green curly arrows indicate the rotation of the Σ dihedral about the C–N single bond. **c**, Portion of the variable-temperature ^{1}H NMR spectra of the PSS mixture obtained upon irradiation of [*E*-**R1**]$^+$ at 365 nm; total concentration of compound [**R1**]$^+$, $C_{R1} = 5.0 \times 10^{-3}$ M, $CDCl_3$, 500 MHz.

the reactivity of [*E*-**R2**]$^+$ under constant illumination is composed of two photoisomerization reactions ($E \rightleftarrows Z_A$ and $E \rightleftarrows Z_B$), two thermal back-isomerization reactions ($Z_A \rightarrow E$ and $Z_B \rightarrow E$) and one thermal interconversion ($Z_A \rightleftarrows Z_B$), as shown in Fig. 3a. The enantiomeric nature of the two *Z* isomers confers them identical reactivity with respect to thermal and photochemical reactions, allowing the system at the steady state to be treated kinetically as a chemical monomolecular triangular reaction network at equilibrium[45]. However, within this scheme, all the forward and backward processes balance out, excluding any possibility for net directional motion[46].

By contrast, the introduction of a fixed chirality element into [*E*-**R2**]$^+$ would lead to the formation of a pair of diastereomers, once coupled to the photogenerated axial chirality of the *Z*-azoimidazolium unit. The different thermodynamic stability of the diastereomers—and their presumably different photochemical reactivity—would then introduce kinetic asymmetry within the reaction network, possibly leading to a net directionality in the cyclic pathway.

Photogenerated dynamic diastereoisomerism, R3

To reach this objective, the molecular structure of the cation [*E*-**R2**]$^+$ was modified by introducing a methyl substituent at the benzylic position and accessing compound [**R3**]$^+$, provided with an enantiopure asymmetric carbon centre (Fig. 4a).

Irradiation of [*E*-**R3**]$^+$ at 365 nm in deuterated chloroform yields the two diastereomers [Z_A-**R3**]$^+$ and [Z_B-**R3**]$^+$, as shown in the ^{1}H NMR

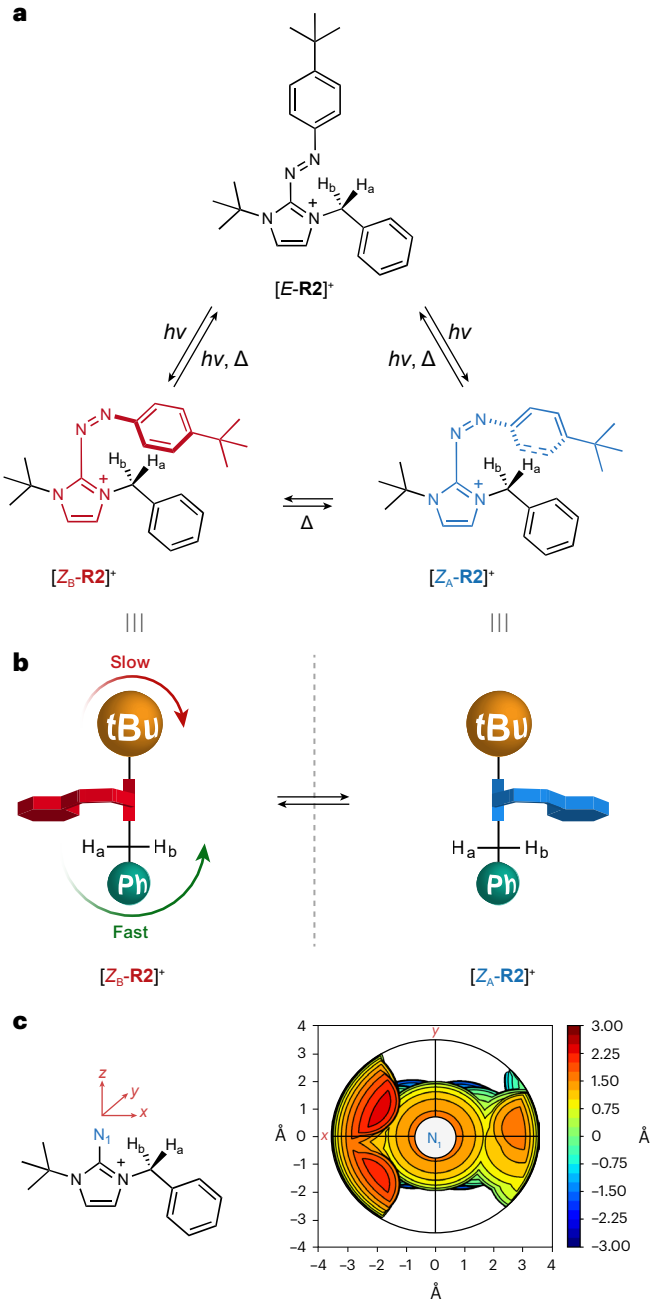

Fig. 3 | Operation of motor [R2]$^+$ and sterically guided dihedral rotation. **a**, Triangular reaction network generated upon irradiation of [*E*-**R2**]$^+$, *hν* = energy of the irradiation wavelength. **b**, Top-view cartoon projections of enantiomers [Z_A-**R2**]$^+$ and [Z_B-**R2**]$^+$. The curly arrows indicate the two possible dihedral rotation pathways leading to their interconversion. **c**, Topographic steric map[57] of the *xy* plane of the stator portion in [*Z*-**R2**]$^+$: according to the colour-coded scale of encumbrance along the *z* axis, the red region on the left highlights the higher steric hindrance of the *tert*-butyl substituent with respect to that of the benzylic group, geometry optimized at the PBE0/aug-cc-pVDZ level.

https://doi.org/10.1038/s41557-025-02045-x

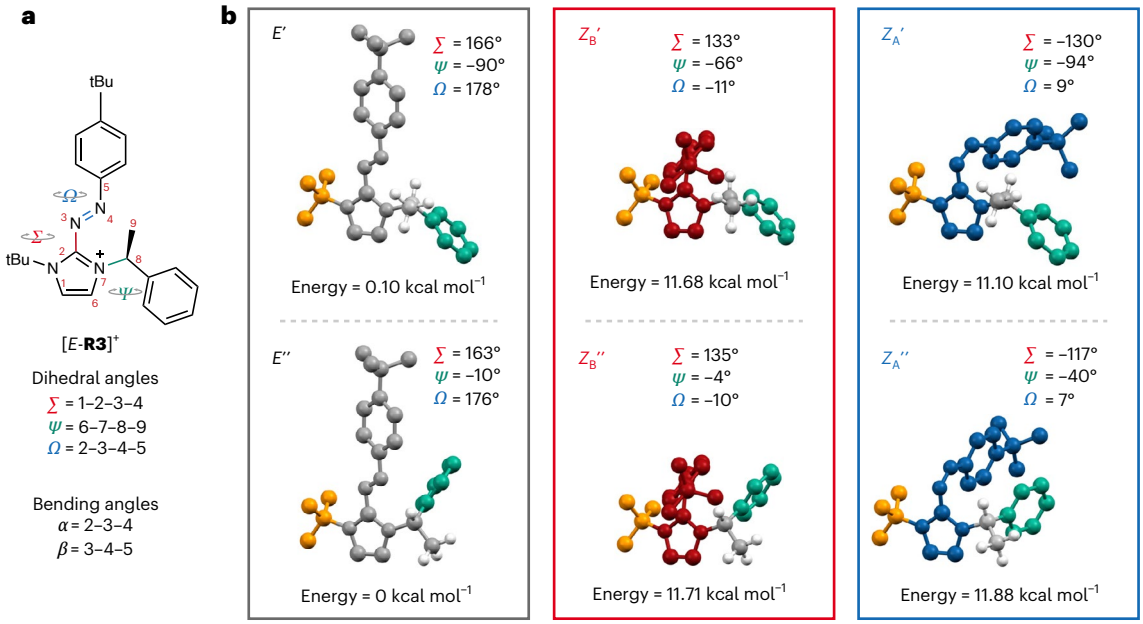

Fig. 4 | Calculated structures of the principal [R3]$^+$ isomers. a, Scanned coordinates depicted on the molecular structure of [*E*-**R3**]$^+$, with definition of the internal coordinates relevant for isomerization. The central bond of each dihedral angle is highlighted with the corresponding colour. **b**, DFT equilibrium structures (PBE0/aug-cc-pVDZ) of the six [**R3**]$^+$ isomers in chloroform associated to the values of the constituent dihedral angles and their relative free energies in kilocalories per mole. For clarity, all hydrogen atoms except those belonging to the benzylic CH and methyl groups have been omitted.

spectrum of the PSS mixture recorded at 218 K, displaying fully resolved resonances for the benzylic proton at 4.39 and 4.13 ppm and *tert*-butyl protons at 1.30 and 1.33 ppm, respectively (Supplementary Fig. 26). The presence of the methyl substituent highly decreases the rate of exchange between [Z_A-**R3**]$^+$ and [Z_B-**R3**]$^+$: in contrast to [*Z*-**R1**]$^+$ and [*Z*-**R2**]$^+$ (Fig. 2 and Supplementary Fig. 25), the resonances proper of the two [*Z*-**R3**]$^+$ stereoisomers do not reach coalescence across a wide temperature range (Supplementary Fig. 27).

The interconversion mechanisms in the absence of light between [Z_A-**R3**]$^+$, [Z_B-**R3**]$^+$ and [*E*-**R3**]$^+$ and their relative stabilities were investigated computationally with the density functional theory (DFT) through a series of ground-state geometry scans performed along the molecular coordinates that are most involved in the isomerization processes (that is, the dihedrals Σ, Ψ and Ω highlighted in Fig. 4a). While Σ drives the [Z_A-**R3**]$^+$ ⇄ [Z_B-**R3**]$^+$ interconversion, Ψ governs the spatial position of the benzylic group with respect to the arylazo unit, and finally Ω, alongside the bending angles α and β, are the main reaction coordinates for the *E* ⇄ *Z* isomerization. The scan of Σ for the *Z*-diazene configurations confirmed the experimental evidence of two minimum energy basins at $\Sigma \approx \pm 130°$ corresponding to the isomers Z_A and Z_B, markedly different in the relative position of the arylazo group. In addition, from the scan of Ψ the presence of more than one conformer for both Z_A and Z_B differing in the benzylic group orientation was detected. The two most stable structures of each *Z* isomer (Z_A'/Z_A'' and Z_B'/Z_B'') have similar energy and are represented in Fig. 4b, whereas the other conformers at higher energy are detailed in Supplementary Fig. 53 and Supplementary Table 2. The different conformations found in the four structures are reflected in the ^{1}H NMR chemical shifts values. In particular, the signals of the methyl and benzylic protons are particularly subjected to the different orientation of the arylazo unit and the benzylic group and are shielded or de-shielded according to the proximity between the two arene rings (Supplementary Table 4). While the difference between Z_A' and Z_A'' mainly arises from the presence of a π-stacking configuration of the latter, for the Z_B couple, it can be observed how the different possible orientations of the benzylic ring cause a more shielded signal at the stereocentre of either the methyl hydrogens (for Z_B') or the benzylic hydrogen (Z_B'') due to the proximity with the arylazo group. Calculations of the chemical shifts fairly reproduce the average shielded chemical shifts observed experimentally for such resonances (Supplementary Fig. 26), thus endorsing the existence of the two Z_B species.

Further DFT scans of the azoimidazolium torsion (Ω) starting from the four *Z* equilibrium structures allowed to identify the existence of a couple of *E* isomers, labelled *E*′ and *E*″, as they differ for the position of the benzyl group ($\Psi \approx -10°$ and $-90°$, respectively). The six main [**R3**]$^+$ conformers are depicted in Fig. 4b, with the corresponding relative free energy values, whereas the zero-point energy and vibrational corrections are reported in Supplementary Table 2 along with the main geometrical parameters. As expected, the *E* isomers are considerably more stable (~10 kcal mol^{-1}) than their *Z* analogues, permitting a unidirectional *Z* → *E* thermal reaction channel with an activation energy of about 20 kcal mol^{-1} (Supplementary Fig. 56). Isomers *E*′ and *E*″ have very similar energy and can easily interconvert, with an estimated barrier of 2 kcal mol^{-1}.

Instead, following the chemical design of the system, the Z_A ⇄ Z_B thermal interconversion has a high activation energy, which in addition depends on the direction of the rotation about the C–N bond (roughly 15 kcal mol^{-1} at $\Sigma = 180°$ and 20 kcal mol^{-1} at $\Sigma = 0°$) (Supplementary Fig. 54). Finally, calculations predict a very similar thermodynamic stability for conformers Z_A and Z_B, and therefore, a relative population close to 1:1 is expected at room temperature.

Light-steered directional motion

The slow rotation of the Σ dihedral observed by variable-temperature NMR spectroscopy and confirmed by DFT simulations prompted an in-depth kinetic analysis of the speciation of [**R3**]$^+$ under illumination and in the dark. Isomerization of [*E*-**R3**]$^+$ under continuous light irradiation at 365 nm monitored by in situ NMR spectroscopy at 218 K shows the gradual formation over time of the two *Z* diastereomers, up to a PSS at which their relative abundance amounts to 57:43 [Z_B-**R3**]$^+$:[Z_A-**R3**]$^+$ (14% diastereomeric excess) (Fig. 5b, violet background). Upon interruption of the illumination, the diastereomers undergo thermal

https://doi.org/10.1038/s41557-025-02045-x

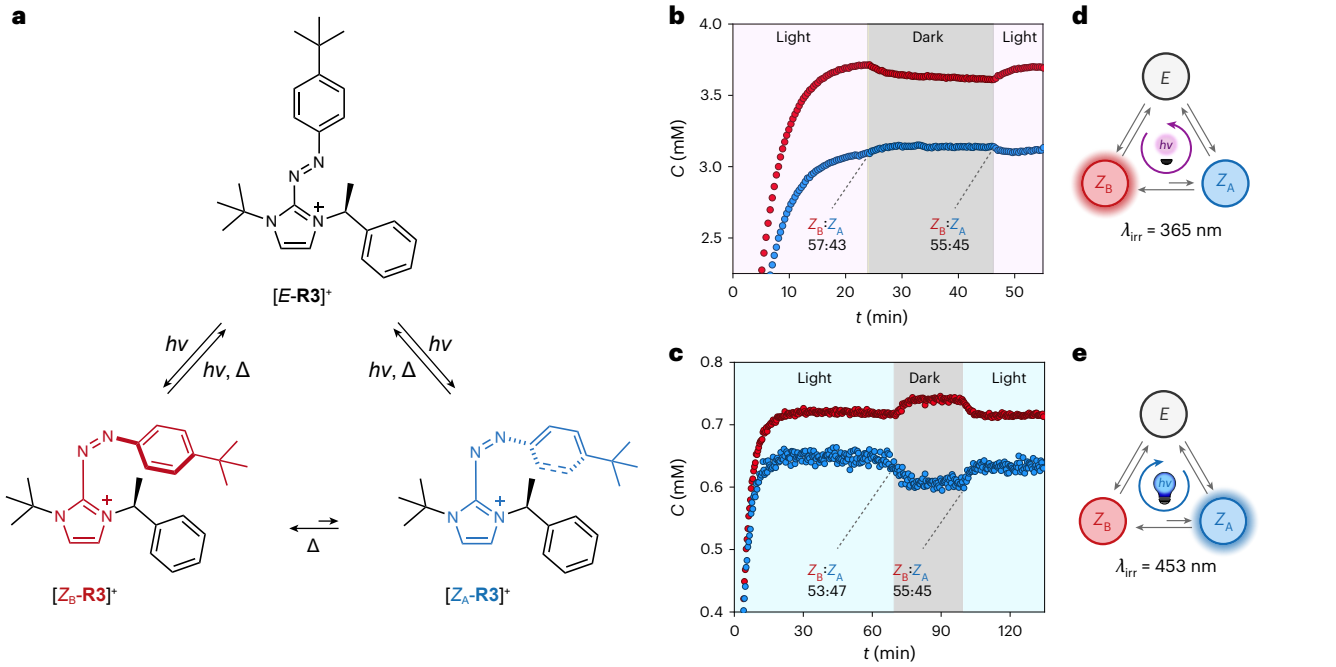

Fig. 5 | Operational network of rotary motor [R3]$^+$ and wavelength-steered net directional motion. a, Triangular reaction network sustained upon irradiation of [*E*-**R3**]$^+$. **b**,**c**, Evolution of [Z_A-**R3**]$^+$ (blue dots) and [Z_B-**R3**]$^+$ (red dots) in the dark (grey background) or upon irradiation at 365 nm (violet background) (**b**) or 453 nm (cyan background) (**c**). **d**,**e**, A schematic representation of the counter-clockwise (**d**) or clockwise (**e**) net directional motion undertaken within the closed reaction cycle, with the two accumulated species highlighted according to the corresponding colour code; ^{1}H NMR, $CDCl_3$, 500 MHz, 218 K; total concentration of compound [**R3**]$^+$, $C_{\mathbf{R3}} = 1.0\times10^{-2}$ M for **b** or 4.8×10^{-3} M for **c**.

equilibration over time reaching a plateau ratio of 55:45 (10% diastereomeric excess) (Fig. 5b, grey background, $\Delta\Delta G = 0.087$ kcal mol^{-1} in favour of Z_B). Fitting of the thermal equilibration data provided the kinetic constant for the [Z_A-**R3**]$^+$ ⇄ [Z_B-**R3**]$^+$ thermal equilibration $k_{ZB\rightarrow ZA} = 3.2\times10^{-3}$ s^{-1} (Supplementary Fig. 31), which through the Eyring equation[47] provides the corresponding activation energy barrier of ~15 kcal mol^{-1} in agreement with the DFT calculated one (Supplementary Fig. 54b). Resuming the 365 nm illumination restores the original 57:43 ratio.

Under constant irradiation the concentrations of [Z_A-**R3**]$^+$ and [Z_B-**R3**]$^+$ are continuously driven away from their equilibrium value; therefore, at the experimental temperature, the thermal interconversion between the diastereomers is slower than their photochemical reactions. The processes leading to the accumulation of the thermodynamically most stable diastereomer [Z_B-**R3**]$^+$ beyond its equilibrium value, namely the forward [*E*-**R3**]$^+$ ⇄ [Z_B-**R3**]$^+$ isomerization and the photochemical [*E*-**R3**]$^+$ ⇄ [Z_A-**R3**]$^+$ back isomerization[48,49], generate kinetic asymmetry within the reaction cycle and determine a net counter-clockwise preferential direction of travel along the cycle, encompassing the sequence (1) [*E*-**R3**]$^+$ → [Z_B-**R3**]$^+$, (2) [Z_B-**R3**]$^+$ → [Z_A-**R3**]$^+$ and (3) [Z_A-**R3**]$^+$ → [*E*-**R3**]$^+$ (Fig. 5d).

Since the travelling directionality is induced by the photochemical branches of the triangular network, their intrinsic dependence on the irradiation wavelength prompted the study of the reactivity of [*E*-**R3**]$^+$ upon visible light illumination, thanks to the presence of n–π* transition bands in the visible region for the three [**R3**]$^+$ isomers (Supplementary Fig. 45). Continuous irradiation of [*E*-**R3**]$^+$ at 453 nm provides a PSS mixture composed of [Z_B-**R3**]$^+$ and [Z_A-**R3**]$^+$ in a 53:47 ratio (6% diastereomeric excess) (Fig. 5c, cyan background). Importantly, mirroring what observed in the previous experiment at 365 nm, suspension of light irradiation led to a thermal equilibration to the 55:45 ratio (Fig. 5c, grey background), whereas the dissipative state could be reached again upon restoring illumination. The accumulation of [Z_A-**R3**]$^+$ with respect to the diastereomer ratio at thermal equilibrium suggests that the provided 453 nm light favours the photochemical [*E*-**R3**]$^+$ ⇄ [Z_B-**R3**]$^+$ back isomerization and/or the forward [*E*-**R3**]$^+$ ⇄ [Z_A-**R3**]$^+$ isomerization compared with their respective reverse process, inducing this time a preferential clockwise travel along the triangular reaction network (Fig. 5e), that is the opposite of what was achieved by illumination at 365 nm. Since under irradiation at both wavelengths each of the three interconverted states is associated to a specific value of the Σ dihedral, the oriented reaction sequence corresponds to a net counter-clockwise (λ_{irr} = 365 nm) or clockwise (λ_{irr} = 453 nm) rotation of the phenyldiazene unit—that is, the rotator—with respect to the imidazolium fragment—that is, the stator.

To ascertain this, the nature of the motion of the phenyldiazene unit during the photoisomerization of [*E*-**R3**]$^+$ was explored with time-dependent density functional theory optimizations in S_1 (corresponding to the excitation at λ_{irr} = 453 nm) and S_2 (λ_{irr} = 365 nm) starting from the [*E*-**R3**]$^+$ equilibrium geometry (Supplementary Fig. 61). The mechanism appears to be similar to that of azobenzene, with an initial decrease of the bending angles (α or β) on S_2 that rapidly leads to the crossing with S_1. Following the decay to S_1, the molecule first undergoes a relaxation of the α and β angles towards larger values (~135°), after which the movement towards the crossing with S_0 at $\Omega \approx 90°$ is predominantly rotational. It can be therefore concluded that, such as azobenzene[50–53] and other azoheteroarenes[54], the phenyldiazene moiety behaves as a rotator upon excitation, regardless of the excitation wavelength. Supplementary Video 1 qualitatively illustrates a full rotation cycle, displaying the sequential interconversion of the three [**R3**]$^+$ isomers along the ground-state potential energy surface.

The extent of the directionality conferred to the rotary motion of [**R3**]$^+$ can be quantified by the ratcheting constant K_r, expressed as the ratio between the product of the rate constants of all the processes occurring within the closed reaction network that go in a direction (clockwise or counter clockwise) and that of the rate constants of all the processes that go in the opposite direction (counter clockwise or

clockwise). According to the labelling detailed in Supplementary Fig. 69, the ratcheting constant can be expressed as

$$K_r = \frac{k_1}{k_{-1}} \times \frac{k_2}{k_{-2}} \times \frac{k_3}{k_{-3}}$$

and can be estimated from the PSS concentrations of the photochemical processes and the equilibrium concentrations of the thermal process[55,56]:

$$K_r = \frac{[Z_A]_{PSS}}{[E]_{PSS}} \times \frac{[Z_B]_{eq}}{[Z_A]_{eq}} \times \frac{[E]_{PSS}}{[Z_B]_{PSS}} = \frac{[Z_A]_{PSS}}{[Z_B]_{PSS}} \times \frac{[Z_B]_{eq}}{[Z_A]_{eq}}.$$

In the adopted irradiation regime, the ratcheting constant results in $K_{r(CW/CCW)} = 0.92$ under UV irradiation and $K_{r(CW/CCW)} = 1.08$ under visible light irradiation, which on average translate into one directional rotation every 12 turns.

Crucially, fast thermal $Z \rightarrow E$ isomerisation processes currently represent the main disadvantage of this system, competing with the light-driven biased travel along the network and partly eroding the net directional bias (Supplementary Fig. 32).

Conclusion

This work introduces a family of readily available arylazoimidazolium photoswitches, which upon light irradiation access *Z* isomers endowed with axial chirality. Starting from the fully symmetric [**R1**]$^+$ and gradually lowering its symmetry through structural variations, the photoisomerization process in compound [**R3**]$^+$ ultimately leads to the generation of diastereomeric *Z* isomers taking part to a triangular stereodynamic reaction network. The different stability and reactivity of the two [*Z*-**R3**]$^+$ isomers induce a preferential counter-clockwise travelling direction within the reaction cycle upon irradiation at 365 nm. The dissipative nature of this state was confirmed by the variation in terms of diastereomeric excess upon suspension of the illumination, leading to the ratio defined by the relative thermodynamic stability of the diastereomers (14% diastereomeric excess at $\lambda_{irr} = 365$ nm versus 10% diastereomeric excess in the dark). Importantly, the system showed a marked dependence on the irradiation wavelength, reversing the net preferential direction of travel along the reaction cycle, thereby also inverting the direction of the rotary motion, upon irradiation with visible light (6% diastereomeric excess at $\lambda_{irr} = 453$ nm versus 10% diastereomeric excess in the dark).

DFT simulations on the [**R3**]$^+$ isomers confirmed the existence of independent energy minima for the *Z* species, separated by a high energy barrier (~15 kcal mol^{-1}), consistent with the slow rotation of the Σ dihedral observed experimentally at 218 K. Moreover, the diazene photoisomerization proceeds according to a predominantly rotational pathway, corroborating the nature of such compound as a light-driven molecular rotary motor. The ability to turn Brownian fluctuations into direction-controlled motion has been the central pillar around which artificial molecular motors were built in the last decades. Nonetheless, the possibility to steer such direction at will by simply tuning the external stimulus provided represented an unsolved challenge so far. Coupling a fixed chirality element with a light-generated one, the presented system ultimately produces a three-stroke rotary motor able not only to travel directionally across space but also to steer its direction by simply switching the wavelength of the light applied. In consideration of the widespread use of diazene derivatives, this work introduces a readily available and effectively applicable alternative to stilbene-based motors, provided with a peculiar ion pair chemical nature and a unique mode of operation. The relevance of the present study goes well beyond the field of artificial molecular machines, as it poses the basis for innovative properties arising from the photoinduced atropisomerism and directional motion in fields such as light-effected chiral ionic liquids, light-directed asymmetric catalysis and biocompatible photocontrolled materials.

Online content

Any methods, additional references, Nature Portfolio reporting summaries, source data, extended data, supplementary information, acknowledgements, peer review information; details of author contributions and competing interests; and statements of data and code availability are available at https://doi.org/10.1038/s41557-025-02045-x.

References

1. Baker, M. A. B. & Berry, R. M. An introduction to the physics of the bacterial flagellar motor: a nanoscale rotary electric motor. *Contemp. Phys.* **50**, 617–632 (2009).
2. Schliwa, M. *Molecular Motors* (Wiley, 2004).
3. Vale, R. D. & Milligan, R. A. The way things move: looking under the hood of molecular motor proteins. *Science* **288**, 88–95 (2000).
4. Brown, A. I. & Sivak, D. A. Theory of nonequilibrium free energy transduction by molecular machines. *Chem. Rev.* **120**, 434–459 (2020).
5. Goodsell, D. S. *The Machinery of Life* (Copernicus, 2009).
6. Aprahamian, I. The future of molecular machines. *ACS Cent. Sci.* **6**, 347–358 (2020).
7. Kassem, S. et al. Artificial molecular motors. *Chem. Soc. Rev.* **46**, 2592–2621 (2017).
8. Astumian, R. D. Kinetic asymmetry and directionality of nonequilibrium molecular systems. *Angew. Chem. Int. Ed.* **63**, e202306569 (2024).
9. Mondal, A., Toyoda, R., Costil, R. & Feringa, B. L. Chemically driven rotatory molecular machines. *Angew. Chem. Int. Ed.* **61**, e20220663 (2022).
10. Erbas-Cakmak, S., Leigh, D. A., McTernan, C. T. & Nussbaumer, A. L. Artificial molecular machines. *Chem. Rev.* **115**, 10081–10206 (2015).
11. Corra, S., Curcio, M., Baroncini, M., Silvi, S. & Credi, A. Photoactivated artificial molecular machines that can perform tasks. *Adv. Mater.* **32**, 1906064 (2020).
12. Baroncini, M., Silvi, S. & Credi, A. Photo- and redox-driven artificial molecular motors. *Chem. Rev.* **120**, 200–268 (2020).
13. Pooler, D. R. S., Lubbe, A. S., Crespi, S. & Feringa, B. L. Designing light-driven rotary molecular motors. *Chem. Sci.* **12**, 14964–14986 (2021).
14. Oruganti, B., Wang, J. & Durbeej, B. Quantum chemical design of rotary molecular motors. *Int. J. Quantum Chem.* **118**, e25405 (2018).
15. Sheng, J. et al. Formylation boosts the performance of light-driven overcrowded alkene-derived rotary molecular motors. *Nat. Chem.* **16**, 1330–1338 (2024).
16. Boursalian, G. B. et al. All-photochemical rotation of molecular motors with a phosphorus stereoelement. *J. Am. Chem. Soc.* **142**, 16868–16876 (2020).
17. Roke, D., Wezenberg, S. J. & Feringa, B. L. Molecular rotary motors: unidirectional motion around double bonds. *Proc. Natl Acad. Sci. USA* **115**, 9423–9431 (2018).
18. Kistemaker, J. C. M. et al. Third-generation light-driven symmetric molecular motors. *J. Am. Chem. Soc.* **139**, 9650–9661 (2017).
19. Koumura, N., Zijlstra, R. W. J., van Delden, R. A., Harada, N. & Feringa, B. L. Light-driven monodirectional molecular rotor. *Nature* **401**, 152–155 (1999).
20. Greb, L., Eichhofer, A. & Lehn, J.-M. Synthetic molecular motors: thermal N inversion and directional photoinduced CN bond rotation of camphorquinone imines. *Angew. Chem. Int. Ed.* **54**, 14345–14348 (2015).
21. Greb, L. & Lehn, J.-M. Light-driven molecular motors: imines as four-step or two-step unidirectional rotors. *J. Am. Chem. Soc.* **136**, 13114–13117 (2014).
22. Gerwien, A., Gnannt, F., Mayer, P. & Dube, H. Photogearing as a concept for translation of precise motions at the nanoscale. *Nat. Chem.* **14**, 670–676 (2022).
23. Wilcken, R. et al. Complete mechanism of hemithioindigo motor rotation. *J. Am. Chem. Soc.* **140**, 5311–5318 (2018).

24. Gerwien, A., Mayer, P. & Dube, H. Photon-only molecular motor with reverse temperature-dependent efficiency. *J. Am. Chem. Soc.* **140**, 16442–16445 (2018).
25. Guentner, M. et al. Sunlight-powered kHz rotation of a hemithioindigo-based molecular motor. *Nat. Commun.* **6**, 8406 (2015).
26. Kuntze, K. et al. A visible-light-driven molecular motor based on barbituric acid. *Chem. Sci.* **14**, 8458–8465 (2023).
27. Filatov, M. et al. Towards the engineering of a photon-only two-stroke rotary molecular motor. *Nat. Commun.* **13**, 6433 (2022).
28. Pooler, D. R. S., Doellerer, D., Crespi, S. & Feringa, B. L. Controlling rotary motion of molecular motors based on oxindole. *Org. Chem. Front.* **9**, 2084–2092 (2022).
29. Perrot, A., Wang, W., Buhler, E., Moulin, E. & Giuseppone, N. Bending actuation of hydrogels through rotation of light-driven molecular motors. *Angew. Chem. Int. Ed.* **62**, e202300263 (2023).
30. Chen, J. et al. Artificial muscle-like function from hierarchical supramolecular assembly of photoresponsive molecular motors. *Nat. Chem.* **10**, 132–138 (2018).
31. Foy, J. T. et al. Dual-light control of nanomachines that integrate motor and modulator subunits. *Nat. Nanotechnol.* **12**, 540–545 (2017).
32. Li, Q. et al. Macroscopic contraction of a gel induced by the integrated motion of light-driven molecular motors. *Nat. Nanotechnol.* **10**, 161–165 (2015).
33. Qutbuddin, Y. et al. Light-activated synthetic rotary motors in lipid membranes induce shape changes through membrane expansion. *Adv. Mater.* **36**, 2311176 (2024).
34. Li, Q., Tan, J. & Sun, T. Light-driven Feringa motors for precision molecular mechanotherapeutics. *Trends Chem.* **5**, 653–656 (2023).
35. Guinart, A. et al. Synthetic molecular motor activates drug delivery from polymersomes. *Proc. Natl Acad. Sci. USA* **120**, e2301279120 (2023).
36. Corra, S., Curcio, M. & Credi, A. Photoactivated artificial molecular motors. *JACS Au* **3**, 1301–1313 (2023).
37. Zhang, Q., Qu, D.-H., Tian, H. & Feringa, B. L. Bottom-up: can supramolecular tools deliver responsiveness from molecular motors to macroscopic materials? *Matter* **3**, 355–370 (2020).
38. Jerca, F. A., Jerca, V. V. & Hoogenboom, R. Advances and opportunities in the exciting world of azobenzenes. *Nat. Rev. Chem.* **6**, 51–69 (2022).
39. Asaka, T., Akai, N., Kawai, A. & Shibuya, K. Photochromism of 3-butyl-1-methyl-2-phenylazoimidazolium in room temperature ionic liquids. *J. Photochem. Photobiol. A* **209**, 12–18 (2010).
40. Borsley, S., Kreidt, E., Leigh, D. A. & Roberts, B. M. W. Autonomous fuelled directional rotation about a covalent single bond. *Nature* **604**, 80–85 (2022).
41. Greenfield, J. L. et al. *Molecular Photoswitches* (ed. Pianowski, Z. L.) Ch. 5 (Wiley, 2022).
42. Lin, I. J. B. & Vasam, C. S. Preparation and application of N-heterocyclic carbene complexes of Ag(I). *Coord. Chem. Rev.* **251**, 642–670 (2007).
43. Nicoli, F. et al. Photoinduced autonomous nonequilibrium operation of a molecular shuttle by combined isomerization and proton transfer through a catalytic pathway. *J. Am. Chem. Soc.* **144**, 10180–10185 (2022).
44. Hugelshofer, C. L., Mellem, K. T. & Myers, A. G. Synthesis of quaternary α-methyl α-amino acids by asymmetric alkylation of pseudoephenamine alaninamide pivaldimine. *Org. Lett.* **15**, 3134–3137 (2013).
45. Onsager, L. Reciprocal relations in irreversible processes. *Phys. Rev.* **37**, 405–426 (1931).
46. Astumian, R. D. Microscopic reversibility as the organizing principle of molecular machines. *Nat. Nanotechnol.* **7**, 684–688 (2012).
47. Uhl, E., Thumser, S., Mayer, P. & Dube, H. Transmission of unidirectional molecular motor rotation to a remote biaryl axis. *Angew. Chem. Int. Ed.* **57**, 11064–11068 (2018).
48. Weingart, O., Lan, Z., Thiel, W. & Thiel, W. Chiral pathways and periodic decay in *cis*-azobenzene photodynamics. *J. Phys. Chem. Lett.* **2**, 1506–1509 (2011).
49. Wang, Y.-T. et al. Photoisomerization of arylazopyrazole photoswitches: stereospecific excited-state relaxation. *Angew. Chem. Int. Ed.* **55**, 14009–14013 (2016).
50. Aleotti, F. et al. Multidimensional potential energy surfaces resolved at the RASPT2 level for accurate photoinduced isomerization dynamics of azobenzene. *J. Chem. Theory Comput.* **15**, 6813–6823 (2019).
51. Nenov, A. et al. UV-light-induced vibrational coherences: the key to understand Kasha rule violation in *trans*-azobenzene. *J. Phys. Chem. Lett.* **9**, 1534–1541 (2018).
52. Casellas, J., Bearpark, M. J. & Reguero, M. Excited-state decay in the photoisomerization of azobenzene: a new balance between mechanisms. *ChemPhysChem* **17**, 3068–3079 (2016).
53. Moghaddam, K. G., Giudetti, G., Sipma, W. & Faraji, S. Theoretical insights into the effect of size and substitution patterns of azobenzene derivatives on the DNA G-quadruplex. *Phys. Chem. Chem. Phys.* **22**, 26944–26954 (2020).
54. Vela, S., Krüger, C. & Corminboeuf, C. Exploring chemical space in the search for improved azoheteroarene-based photoswitches. *Phys. Chem. Chem. Phys.* **21**, 20782–20790 (2019).
55. Corra, S. et al. Kinetic and energetic insights into the dissipative non-equilibrium operation of an autonomous light-powered supramolecular pump. *Nat. Nanotechnol.* **17**, 746–751 (2022).
56. Sangchai, T., Al Shehimy, S., Penocchio, E. & Ragazzon, G. Artificial molecular ratchets: tools enabling endergonic processes. *Angew. Chem. Int. Ed.* **62**, e202309501 (2023).
57. Falivene, L. et al. Towards the online computer-aided design of catalytic pockets. *Nat. Chem.* **11**, 872–879 (2019).

Methods

General details and synthetic methods are reported in Supplementary Information.

NMR Irradiation experiments

^{1}H NMR spectra were recorded on an Agilent DD2 spectrometer operating at 500 MHz or a Varian Mercury spectrometer operating at 400 MHz. ^{13}C NMR spectra were recorded on an Agilent DD2 spectrometer operating at 126 MHz or a Varian Mercury spectrometer operating at 101 MHz. ^{19}F NMR spectra were recorded on an Agilent DD2 spectrometer operating at 470 MHz. Chemical shifts are quoted in parts per million relative to tetramethylsilane ($SiMe_4$, $\delta = 0$ ppm), using the residual solvent peak as a reference standard; all coupling constants (J) are expressed in Hertz (Hz). The samples were irradiated directly inside the thermostated NMR probe, using a 1 mm silica core optical fibre (Thorlabs) connected to a Prizmatix UHP-T-365-SR LED Illuminator (1.5 W, $\lambda_{max} = 369$ nm, full width at half maximum, 15.56 nm) or a Led Engin LZ1-00B202 LED Illuminator (3.3 W, $\lambda_{max} = 453$ nm, full width at half maximum, 14.59 nm) through an FCA-SMA (Fiber-optic Connector for Angled physical contact SubMiniature version A) adaptor. At its other end, the protective coating of the optical fibre was removed (about 6 cm), and the exposed fibre was sanded to enable the diffusion of light from the fibre core into the solution. The fibre prepared in this way was immersed directly into the thermostated solution (550 µl of 10 mM or 5 mM solution of the motor) in the NMR tube. The obtained experimental data were processed using the software MestReNova and OriginPro 2019.

UV–visible light irradiation experiments

Absorption spectra were recorded on a Perkin Elmer Lambda750 double beam spectrophotometer using 10 mm pathlength quartz cuvettes (Hellma). Irradiation experiments were performed on air equilibrated solutions, thoroughly stirred, using a medium pressure Hg lamp (200 W) at room temperature. The Hg lamp was also coupled with an Avantes StarLine AvaSpec-ULS2048CL-EVO-RS spectrophotometer to collect absorption spectra with high rates under continuous irradiation. The spectrophotometer was equipped with an optical fibre which enables the fast acquisition of absorption spectra (ms) and concomitant in situ irradiation. The desired wavelength of irradiation was selected using an appropriate interference filter. The incident photon flux of the irradiation lamp was determined to be 4.4×10^{-9} Einstein s^{-1}, 2.8×10^{-9} Einstein s^{-1} and 4.3×10^{-9} Einstein s^{-1}, respectively, at 365 nm, 405 nm and 436 nm, using the 4,4′-dimethylazobenzene actinometer. The absorption spectra of the unknown Z isomers were extrapolated mathematically, according to the method reported by Fischer in 1967. The photoisomerization quantum yields ($\Phi_{E\to Z}$) were determined from the disappearance of the π–π* band of the azoimidazolium unit by fitting the initial part of the global photokinetic taking into account just low conversion percentages (<10%) and the thermal back-isomerization contribution. This choice was required by the need to consider negligible the quantum yield of the photochemical back-isomerization processes ($\Phi_{Z\to E}$), since only mathematically extrapolated absorption spectra of pure Z isomers could be obtained for the investigated molecules. Determination of $\Phi_{Z\to E}$ was also attempted, but the high uncertainty on the molar absorption coefficient of the Z form prevented its accurate assessment. The fraction of light transmitted at the irradiation wavelength was taken into account in the calculation of the quantum yields. The fitting was performed using the software Berkeley Madonna. The rate constants for thermal back-isomerization reactions were obtained by fitting the back-isomerization spectral data at the maximum wavelength against time using a first-order kinetics (exponential) model in OriginPro 2019.

Computational details

Internal coordinate scans and excited states calculations were performed at DFT or time-dependent density functional theory level using the Gaussian16 software. The final energies and geometries of all scanned structures were obtained with the PBE0 hybrid functional coupled with the aug-cc-pVDZ basis set and Grimme's dispersion corrections (D3BJ). $CHCl_3$ solvent contribution was introduced through the polarizable continuum model. The results were compared with CASPT2 gas phase calculations and BHHLYP, M06-2X and wB97XD calculations in gas phase and implicit solvent (Supplementary Tables 5–9). The same software was used to simulate the absorption spectra of all minima and rotational transition states with the aug-cc-pVDZ basis set and PBE0, M06-X, wB97X-D and BHHLYP functionals. The results are reported in Supplementary Figs. 59 and 60 and Supplementary Tables 10–13.

The ORCA software was employed for the DFT calculation of the ^{1}H NMR chemical shifts of all conformers reported in Fig. 4, using the PBE0 functional and the pcSseg-2 basis set and, again, polarizable continuum model. The reported chemical shifts (Supplementary Table 4) represent the shift with respect to calculated resonant frequencies for tetramethylsilane and were averaged among the chemically equivalent protons.

The geometries of the S_2/S_1 and S_1/S_0 conical intersections were optimized at CASPT2 level with the aug-cc-pVDZ basis set in explicit solvent (chloroform) employing the quantum mechanics/molecular mechanics (QM/MM) scheme available in COBRAMM, interfaced with OpenMolcas and AMBER for the QM and MM calculations, respectively. The gas phase energies of the ground-state minima and conformers, as well as the ground-state transition states, were computed with the same methodology. More details on the CASPT2 calculations, including active space orbitals, are available in Supplementary Information.

Data availability

The online version of this Article provides Supplementary Information, including Supplementary Figs. 1–69, general methods, detailed experimental and analytical data, NMR spectra, UV–visible light spectra, computed geometries, NMR chemical shifts and ground and excited state potential energy surfaces, as well as all the additional supporting data for the study. A movie illustrating the directionally biased isomer interconversion at the ground state, experimental and mathematically extrapolated UV–visible light absorption spectra, NMR photokinetic concentration profiles, coordinates of optimized minima, transition states and minimum energy crossing points, input files for minimum energy crossing points optimizations and energies and oscillator strengths of the excited states for minima and transition states computed with multiple DFT functionals and at the CASPT2 level are provided as additional Supplementary Information.

Acknowledgements

This work was financially supported by the Royal Society of Chemistry (M.C., Research Fund R23-8129362510), the European Union—Next Generation EU and the Italian Ministry of University and Research (A.C., PRIN grant no. 2022JMTLE; M.B. and C.T., PRIN grant no. 2022KMMAYM_002; S.S., PRIN grant no. 201732PY3X; M.G. and F.A., PRIN grant no. P20224AWLB) and the University of Bologna. Correspondence should be addressed to M.C.

Author contributions

M.C. and F.N. conceived the project. M.C., M.B., S.S. and L.M. guided and supervised the research. F.N., S.B. and M.C. synthesized the compounds and carried out NMR experiments. C.T. carried out the photophysical characterisations. E.L. and F.A. conducted computations. A.C., M.B., M.C., S.S. and M.G. secured research funds. M.C., C.T., F.N., E.L. and L.M. wrote the paper. All authors discussed the results and commented the paper.

Competing interests

The authors declare no competing interests.

Additional information

Supplementary information The online version contains supplementary material available at https://doi.org/10.1038/s41557-025-02045-x.

Correspondence and requests for materials should be addressed to Luca Muccioli, Massimo Baroncini or Massimiliano Curcio.

Peer review information *Nature Chemistry* thanks Stefano Crespi, Jin Wen and the other, anonymous, reviewer(s) for their contribution to the peer review of this work.